Edge sheared flows and the dynamics of blob-filaments

J. R. Myra,[1] W. M. Davis,[2] D. A. D'Ippolito,[1] B. LaBombard,[3]
D. A. Russell,[1] J. L. Terry,[3] and S. J. Zweben[2]

[1] Lodestar Research Corporation, Boulder, CO, USA
[2] Princeton Plasma Physics Laboratory, Princeton, NJ, USA
[3] Massachusetts Institute of Technology, Cambridge MA, USA

Dec. 2012

submitted to *Nuclear Fusion*

DOE-ER/54392-71; DOE-ER/54678-8 LRC-12-153

LODESTAR RESEARCH CORPORATION
2400 Central Avenue
Boulder, Colorado 80301

Edge sheared flows and the dynamics of blob-filaments

J. R. Myra,[1] W. M. Davis,[2] D. A. D'Ippolito,[1] B. LaBombard,[3]
D. A. Russell,[1] J. L. Terry,[3] and S. J. Zweben[2]

[1] Lodestar Research Corporation, Boulder, CO, USA
[2] Princeton Plasma Physics Laboratory, Princeton, NJ, USA
[3] Massachusetts Institute of Technology, Cambridge MA, USA

The edge and scrape-off-layer (SOL) region of a tokamak plasma is considered, with emphasis on sheared flow generation and the dynamics of blob-filaments. Both numerical simulations and experimental data analysis are employed. The simulations use the fluid-based 2D curvature-interchange model embedded in the SOLT code. A blob-tracking algorithm based on 2D time-resolved images from the gas puff imaging diagnostic has also been developed and applied to NSTX, Alcator C-Mod and simulation data. The algorithm is able to track the blob motion and changes in blob structure, such as elliptical deformations, that can be affected by sheared flows. Results of seeded blob simulations and quasi-steady turbulence simulations are compared with the experimental data to determine the role of plasma parameters on the blob tracks and to evaluate the exchange of momentum between the blobs and flows. The simulations are shown to reproduce many qualitative and quantitative features of the data including size, scale-length and direction of perpendicular (approximately poloidal) flows, the inferred Reynolds acceleration and residual stress, poloidal reversal of blob tracks, and blob trapping and/or ejection. Mechanisms related to blob motion, SOL currents and radial inhomogeneity are shown to be sufficient to explain the presence or absence of mean and oscillating zonal sheared flows in selected shots.

PACS: 52.30.-q *Plasma dynamics and flow*, 52.35.Ra *Plasma turbulence*, 52.35.We *Plasma vorticity*, 52.55.Fa *Tokamaks, spherical tokamaks*, 2.65.-y *Plasma simulation*

1. Introduction

Sheared flows play an important role in regulating turbulence in fusion plasmas. [1] Furthermore, it has been known for some time that radial inhomogeneity provides a mechanism for sheared flow generation by the turbulence [2, 3]. Here, we consider the interaction of edge and scrape-off-layer (SOL) sheared flows with coherent turbulent structures, i.e. blob-filaments, [4, 5], focusing on the generation of flows, the dynamics of the blob-filaments and their mutual interaction. We define a blob-filament (or simply "blob") to be any filamentary field-aligned structure of significantly enhanced pressure in the edge or SOL region. Because coherent structures are readily observed in the edge plasma using diagnostics such as gas puff imaging (GPI) [6-8], the present approach enables a new kind of comparison of edge turbulence theory with data.

The work is motivated by several considerations. Edge sheared flows, both mean flows and oscillating zonal flows, are believed to be important for the L-H, and H-L transitions [9-19], and an improved understanding of their role will be required for a theory-based scaling of these transitions for ITER and future devices. Theoretical work predicts that the L-H transition can be described by predator-prey models [9, 10], and some recent experimental findings have confirmed many qualitative and some quantitative aspects of the predator-prey paradigm [15-19]. Flow generation by turbulence also implies forces and torques on the plasma which are of interest for understanding bulk plasma rotation.

Another motivation comes from the behavior of blob-filaments in the SOL. Blob generation and dynamics impact both the (near-separatrix) SOL width critical for ITER power handling in the divertor [20, 21], and far SOL interaction with plasma-facing components, which is also an important concern. Turbulent blob interactions near the separatrix generate flows, but the subsequent motion and structure of blob-filaments is also influenced by the sheared flows that they propagate through [22-26]. In some experiments, bursty transport, Reynolds accelerations and edge flows have been shown to be linked. [12, 13, 27-29] The role of blob and eddy tilting, also recently investigated in other studies [30- 32], will be examined as both as a theoretical mechanism and a diagnostic of Reynolds stress in particular experimental discharges.

We will show that edge density and temperature gradients (specifically the profile of the diamagnetic velocity) and changes in edge topology at the separatrix, combined with SOL currents, are sufficiently large to explain the generation of flows observed in two experimental shots. While Reynolds stress in the presence of background sheared $\mathbf{E}\times\mathbf{B}$ flows leads to further flow generation, we will show that there is a symmetry breaking effect – a natural direction for the flows in the absence of a background $\mathbf{E}\times\mathbf{B}$ flow. This symmetry breaking from edge profiles and SOL current flow considerations implies a residual Reynolds stress. The present mechanism

is different from, and presumably acts in addition to, a magnetic-shear induced residual Reynolds stress that has been recently investigated. [33]

Our study of the origin of sheared flow generation and its relation to blob-filament dynamics is greatly facilitated by a new analysis tool for tracking the motion and changes in structure of blobs, namely, a blob-tracking algorithm [34] based on 2D time-resolved images from the GPI diagnostic. This tool and sample results are discussed in Sec. 2. In Sec. 3 we consider some mechanisms for the generation of flows that are related to blob motion, SOL currents and radial inhomogeneity. The SOLT code [35] simulation model and simulation method are described in Sec. 4 together with the results of seeded blob and turbulence simulations for parameters relevant to NSTX and Alcator C-Mod shots. A detailed quantitative comparison of model results with experimental results is given. We also discuss the elliptical deformation of blob structures and a resulting proxy for the Reynolds stress. The net force on the tokamak plasma due to the turbulent momentum escaping across the separatrix is also considered. Finally, our conclusions are given in Sec. 5.

2. Experimental diagnostics and analysis methods

Gas-puff imaging is a valuable diagnostic for the detection of edge turbulent structures and the analysis of their motion. A detailed description of the diagnostic is given elsewhere. [6-8] The basic idea is that a small amount of neutral gas (usually deuterium or helium) is puffed into the edge plasma at a particular toroidal location. The line emission from the gas, which depends on the local plasma density and temperature, is then detected and recorded by a high framing rate camera. In the present study, the camera is positioned to view the motion of the turbulent structures in the plane perpendicular to the magnetic field B. In the present datasets, a 64×64 pixel GPI image frame was captured every 2.5 μs for a total of 20 ms.

A sequence of sample processed frames from NSTX is shown in Fig. 1 for the normalized GPI intensity, i.e. the local intensity I(x, y, t) normalized to the time averaged intensity $\langle I(x, y)\rangle_t$. In Fig. 1 the time interval used for the preceding average was 10 ms. For each local maximum in the frame meeting specified filtering criteria, an ellipse is fit to the half-maximum contour level. The motion of the central maximum and changes in the elliptical fit are tracked from frame to frame. [34] The allowed displacement of a given turbulent structure between frames is restricted (typically to 10 pixels) to distinguish different structures. The structure is considered to be a blob if it meets these criteria and has a sufficient lifetime (typically taken as more than 25 μs). Note that this rather general definition of a blob can include

wave crests inside the separatrix as well as isolated filamentary structures that have been ejected into the SOL.

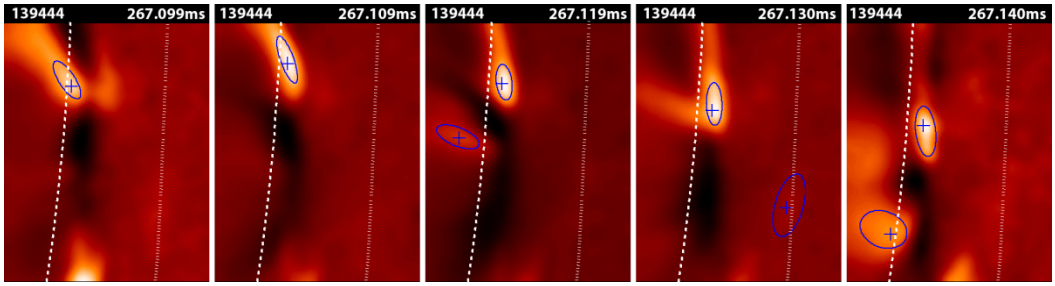

Figure 1. Normalized (see text) GPI intensity for sample frames from NSTX with the palette scaled to the maximum and minimum for each frame. The tokamak Z coordinate is vertical (approximately poloidal); R is horizontal (approximately radial). The time between illustrated frames here is 10 μs (every 4th camera frame). The core plasma is to the left and the dashed line is the approximate (EFIT) separatrix location. The dotted line at right locates a radial limiter. The ellipses are fit by the tracking algorithm and the cross is the location of the maximum brightness within the blob. Note the overall trajectory of the bright blob and the significant elliptical distortion near the separatrix.

In this paper we analyze two shots from the NSTX and Alcator C-Mod experiments. Parameters for these discharges are given in Table I. Both are Ohmic plasmas; the NSTX case is preheated by neutral beams. Of particular note is the difference in the SOL collisionality parameter [5] $\Lambda = \nu_{ei} L_{||}/(\Omega_e \rho_s)$, a point to which we will return. A set of superimposed blob tracks from 3 ms of GPI data in NSTX is shown in Fig. 2. The fitted ellipses (starting one filled) are drawn with the same minor radius regardless of blob size (for visual clarity) and only a portion of the approximately 25×30 cm^2 camera image is shown. The separatrix position is shown by a dashed line. Some blob tracks show outward motion (ejection), some are confined to the edge region (here defined as inside the separatrix). The motion of the edge structures is upwards, which corresponds to the electron diamagnetic direction. Some blob tracks show reversal of the poloidal (approximately vertical) velocity near the separatrix indicating the action of a downward accelerating force. The dominant motion in the SOL is downward, in the ion diamagnetic direction. One of the main goals of this paper is to understand and quantify the mechanisms responsible for the observed blob motion in the y (binormal, approximately poloidal) direction, i.e. the origin of perpendicular sheared flows.

Table 1. Experimental parameters for the NSTX and Alcator C-Mod shots analyzed in this paper. Note especially the large difference in collisionality.

	NSTX Shot 139444	C-MOD Shot 1100824017
$n_{e,sep}$ (m^{-3})	5.8×10^{18}	1.0×10^{20}
$T_{e,sep}$ (eV)	19	47
$\rho_{s,sep}$ (cm)	0.26	0.025
$\Lambda_{SOL} \sim \nu_{e*}(m_e/m_i)^{1/2}$	0.3 – 0.8	1 – 3
blob size $\delta_{b,sep}$ (cm)	2.2 ± 0.5	0.4 ± 0.1
$\delta I/\langle I \rangle\|_{sep}$	< 1.6	< 0.6
GPI gas	D	He
GPI imaging area	25×30 cm^2	5.9×5.9 cm^2

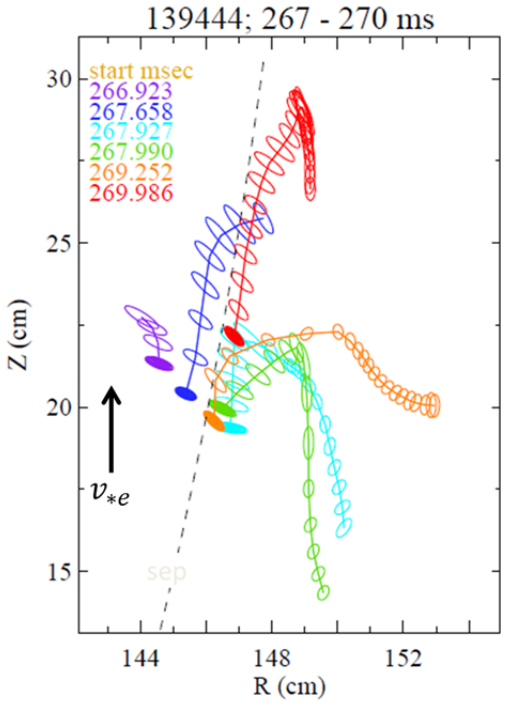

Figure 2. Superposition of selected NSTX blob tracks collected in a 3 ms time interval. All the indicated tracks start in a small region near the filled ellipses. Start times for each track are given in the inset. The electron diamagnetic drift direction is up, and the EFIT separatrix is shown with a dashed line.

3. Mechanisms for blob motion and sheared flow generation

Blob motion is controlled by polarization charges. The basic outward motion results from grad-B and curvature drifts which charge polarize the blob and cause it to **E**×**B** drift [4, 5] as illustrated in Fig. 3a). Background flows or drifts can rotate and shear the blob charge dipole, converting radial motion to partly poloidal motion [36]; see Fig. 3b). If there is a net monopole component to the charge or vorticity, then this implies blob rotation, Fig. 3c), which when superimposed on the basic dipole also gives rise to dipole rotation. A monopole component can arise for a number of reasons. One is that currents flow to sheaths in the SOL, Fig. 3d), to neutralize the blob charge dipole, and excess electrons are lost more easily than excess ions. This is due to the asymmetry of the sheath current-voltage relation.

In general, strong radial inhomogeneity present in the edge and SOL region of a tokamak plasma leads to many mechanisms for sheared flow generation and its interaction with turbulence. These mechanisms are all related to shearing and rotation or tilting deformations of the turbulent structures (called "blobs" here both inside and outside the separatrix). The primary mechanisms can be enumerated as follows:

1) radial variation of the wave group velocity [2, 3] on the scale of the blob radius due to steep profiles and or rapid changes in topology across the separatrix which shear and rotate the blob charge dipole, converting radial blob motion into poloidal motion;
2) a net monopole blob potential due to adiabatic electron physics ($\delta n \sim \delta\Phi$) which induces rotation of the blob charge dipole, [37] mixing radial and poloidal blob motion;
3) asymmetry in the positive and negative parallel currents in the SOL (due to the asymmetry of the sheath current-voltage relation) which causes the blob to charge positive and partially rotate, again converting radial motion into poloidal motion; [38]
4) blob rotation as a sheath-connected blob enters the SOL due to finite blob T_e which induces an internal blob radial electric field; [24]
5) interaction of the blob with an existing strong **E**×**B** shear layer leading to vortex merging and charge dynamics: positive and negative regions of the blob charge dipole are repelled or attracted by regions of vorticity (charge) in the shear layer.

Some of these mechanisms have well-known counterparts in traditional nonlinear Fourier-wave theory [2, 3], but it is illuminating to see them at play in the context of coherent blob structures. Moreover, blob structures are readily detectable by the GPI diagnostic enabling an entirely new kind of comparison between theory and experiment. The five mechanisms listed above are included in the SOLT code simulations which are described next.

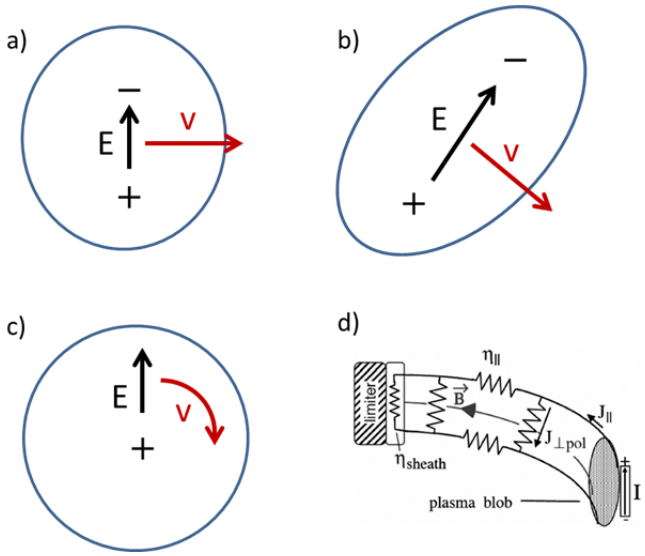

Figure 3. Schematic of mechanisms governing blob motion and blob generation of flows.

4. Simulations and comparison with experiment

A. Simulation model and Reynolds stress analysis

Simulations described in this paper were carried out with the Scrape-Off-Layer Turbulence (SOLT) code [35]. SOLT is a fluid code that models turbulence in the two-dimensional (2D) plane (x, y) perpendicular to the magnetic field $\mathbf{B} = B\mathbf{e}_z$ at the outboard midplane of the torus. Here $x = \Delta r$ is radial distance measured from the separatrix, and y is binormal (approximately poloidal). SOLT implements classical parallel physics using closure relations [4, 39] for the midplane parallel current and parallel fluxes of particles and energy for collisional regimes ranging from sheath-connected to conduction limited. The SOLT code can describe arbitrarily strong nonlinear plasma dynamics ($\delta n/n \sim 1$), including blob formation, and the physics model supports interchange-type curvature-driven modes, sheath and Kelvin-Helmholtz instabilities, and drift waves. Details of the SOLT model have been discussed elsewhere and are summarized in Appendix A. The present version assumes cold ions. SOLT also includes the self-consistent evolution of zonal (i.e., poloidally-averaged) flows. For comparison with experimental GPI data, SOLT employs a synthetic GPI diagnostic to simulate both He and D gas puffs.

SOLT was used for both seeded blob simulations and quasi-steady turbulence simulations of the NSTX and Alcator C-Mod shots. The seeded blob simulations were run as SOLT initial value problems. Smoothed experimental plasma profiles of density and temperature, shown in

Fig. 4, were employed together with other machine parameters that enter the SOLT model: magnetic field B, major radius R, and connection length profile $L_{||}$. Dissipation parameters (plasma viscosity and flow damping) were treated as ad-hoc input parameters since experimental values were not known. Typical blob spatial sizes, amplitudes, and birth locations were extracted from the experimental dataset. A Gaussian blob with the given properties was then superimposed on the back-ground plasma profiles as an initial condition for the SOLT simulation. The blob was tracked until it either disappeared (lost its structure) or travelled radially to a limiter in the far SOL. An example of the resulting synthetic GPI images is shown in Fig. 5.

Additionally, simulations were allowed to run to a quasi-steady turbulent state. These turbulence simulations required the addition of sources to maintain the profiles close to experimental values. Radial electric fields and hence **E**×**B** binormal (y-directed) flows were allowed to build up self-consistently from the turbulent dynamics.

In each simulation case, as well as in the experiments, it is possible to identify individual blob tracks and fit smoothed trajectories to the positions x(t) and y(t). Differentiating with respect to time, one obtains

$$\left\langle a_y \right\rangle = \left\langle \frac{dv_y}{dt} \right\rangle = \left\langle \mathbf{v}\cdot\nabla v_y \right\rangle = \frac{\partial}{\partial x}\left\langle v_x v_y \right\rangle \qquad (1)$$

where the quantities $\langle a_y \rangle$ and $\langle dv_y/dt \rangle$ are computed from averages of "single-particle" blob trajectories while $\left\langle \mathbf{v}\cdot\nabla v_y \right\rangle$ and $\partial_x \left\langle v_x v_y \right\rangle$ are regarded as statistically averaged fluid quantities in the turbulent steady state.

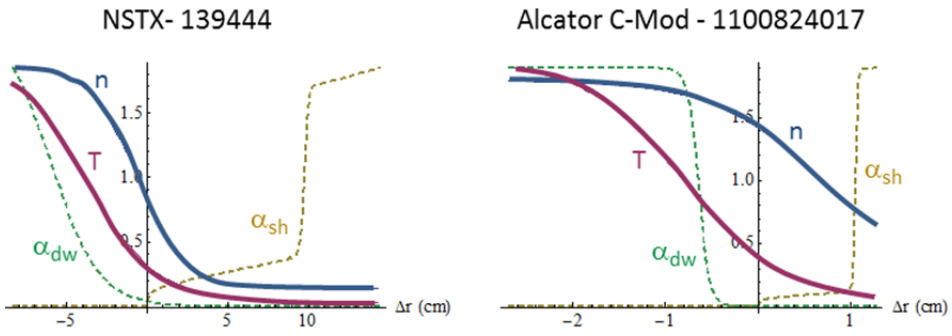

Figure 4. Smoothed normalized background profiles at the outboard midplane of density n and electron temperature T, employed in the SOLT code simulations of the shots described in Table 1. Here the reference (normalization) values for NSTX are $n_0 = 7.0\times10^{12}$ cm^{-3} and $T_0 = 60$ eV; for C-Mod they are $n_0 = 7.3\times10^{13}$ cm^{-3} and $T_0 = 115$ eV. Also shown in dashed lines are the spatial variation of the normalized electron adiabaticity parameter α_{dw} in the edge and the normalized sheath conductivity α_{sh} in the SOL (see Appendix A for definitions).

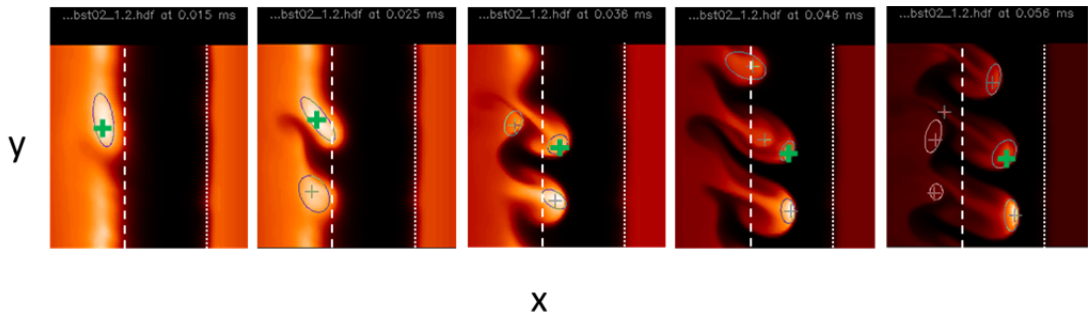

Figure 5. SOLT code simulated normalized GPI image of a seeded blob for the NSTX shot. The vertical coordinate y is binormal (approximately poloidal); x is radial. The time between frames is 10 μs. The core plasma is to the left and the dashed line is the separatrix location; the dotted line is the radial limiter. The green cross marks the seeded blob, which also triggers a secondary blob ejection.

B. Trajectory analysis for seeded blobs

Trajectories for six cases, relevant to the NSTX discharge are shown in Fig. 6. Fig. 6a) is a representative NSTX track obtained by initializing the blob with the mean blob parameters of Table 1, and using experimental outer midplane plasma profiles and parameters for other simulation inputs, except that *no mean background flow is imposed*. Thus the v_y of the blob is generated entirely by blob interaction with the plasma and geometry. This track exhibits blob ejection and v_y reversal similar to the some of the experimental tracks of Fig. 2. It is consistent with other experimental data [40] which typically show flows in the electron diamagnetic direction inside the separatrix, reversing to the ion direction in the SOL. The inferred size (amplitude) of the radial and poloidal blob velocities in the edge and SOL are within a factor of two of the experimental values, the directions are the same, and the scale lengths of variation are similar.

Next in SOLT we artificially varied simulation parameters and physics to infer the importance of specific mechanisms in the experimental data. Fig. 6b) illustrates the track for a completely sheath-connected case (zero collisionality), while Fig. 6c) is for a completely sheath-disconnected case (large collisionality, no parallel current). We infer that parallel currents in the SOL are important in establishing the blob track and the y-acceleration along the track. Fig. 6d) shows the result of suppressing electron adiabatic effects (i.e. $\alpha_{dw} = 0$), and hence the upward electron drift, in the edge region. This blob maintains a stronger dipole charge than the previous case (because adiabatic electrons neutralize the charges by parallel current flow) and is therefore ejected rapidly. It moves downward in the SOL due to the asymmetry of the sheath current-

voltage relation, which favors electron loss. [38] (Ion current in the SOL is limited by the ion saturation current.)

Figs. 6e) and 6f) show the result of imposing a mean background **E**×**B** flow in the SOL, respectively up in 6e) and down in 6f). The imposed Gaussian-shaped flow is approximately confined to and centered in the shaded region. This background flow has a shear and vorticity, which induces a bipolar charge layer (through its $\nabla^2\Phi$) with which the blob charge must interact. For the direction of flow in 6e) the charge layer facing the edge region (i.e. near and just outside the separatrix) is negative. The blob however has acquired a net positive charge through electron adiabaticity [37] in the edge region. (The blob's net positive δn implies a net positive $\delta\Phi$.) Therefore, the blob in 6e) is attracted from the edge to the separatrix and experiences an enhanced ejection. This case is that of counter-shear vortex interaction. When the flow is reversed as in Fig. 6f) the edge blob is repelled from the separatrix and experiences trapping or enhanced confinement. This case is that of co-shear vortex interaction. The sense of the flow shear in 6f) is like the mean flow observed in NSTX (see Fig. 8); this sheared flow acts to enhance edge confinement, and is the blob realization of the well-known mechanism of sheared-flow suppression of turbulence. [3, 41] It is also qualitatively in accord with other NSTX experimental data [42] which showed that blob ejection is suppressed in H-mode, where large sheared flow are present. The size of the flows applied in Figs. 6 e) and f) is comparable to the largest flows seen in the experimental data for this shot.

Note the implications for residual ($v_E = 0$) stress: in cases a) – d) the background **E**×**B** flows were suppressed yet Reynolds acceleration, defined in Eq. (1), still occurs; moreover, response to imposed **E**×**B** flows in e) and f) is asymmetric. Thus the charge dynamics of filamentary structures near the separatrix illustrated in the sketches of Fig. 3 and the simulations of Fig. 6 constitute significant mechanisms for residual stress.

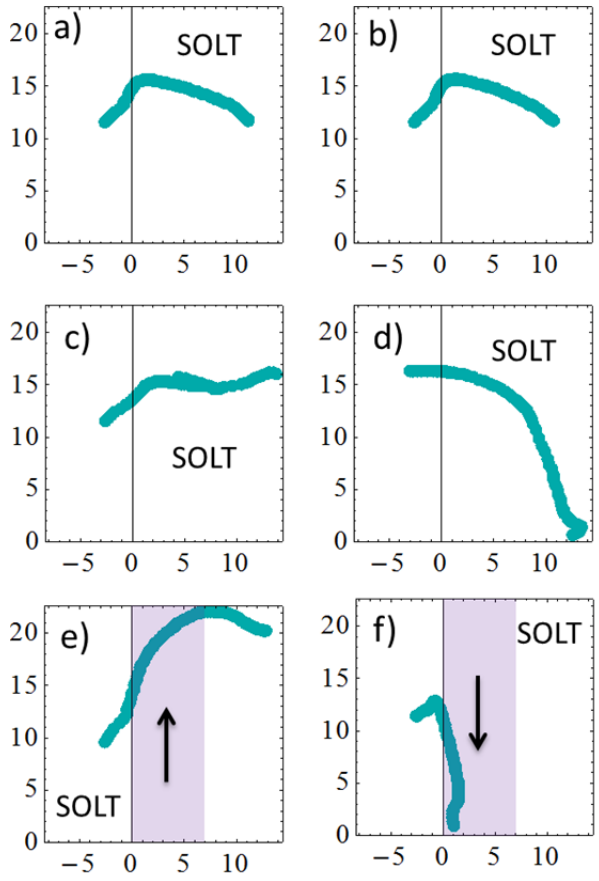

Figure 6. SOLT code seeded blob tracks for the NSTX analysis: a) base, b) fully sheath connected, c) sheath disconnected, d) electron adiabaticity and drifts off, e) imposed SOL $v_{Ey} > 0$, e) imposed SOL $v_{Ey} < 0$.

C. Simulation comparisons for NSTX

An experimental database of blobs for the NSTX shot was obtained, consisting of approximately 4,000 individual blob images (after filtering for an amplitude threshold of $\delta I/I > 0.6$, blob lifetimes > 25 μs, blob half-max area > 6 cm^2). This database resulted in about 400 blob trajectories that could be used in the analysis described by Eq. (1). In Fig. 7, results of this experimental database are compared with the base case seeded blob simulation discussed previously.

For the NSTX shot, the seeded blob simulation (red curve) does a remarkable job of modeling the experimentally observed mean acceleration, indicated by the thick grey region. (The red dashed portion of the blob simulation is the result of an initial transient as the seeded blob relaxes.) As for Fig. 6a), this blob was initialized with the mean blob parameters of Table I,

and evolved using experimental outer midplane plasma profiles and parameters. The satisfying agreement obtained here is the most direct piece of evidence supporting our claim that the simulated mechanisms, specifically the edge electron diamagnetic velocity profile and changes in edge topology at the separatrix, combined with SOL currents, are sufficiently large to explain the Reynolds stress observed in the experiment. Figure 7 is a key result of our paper.

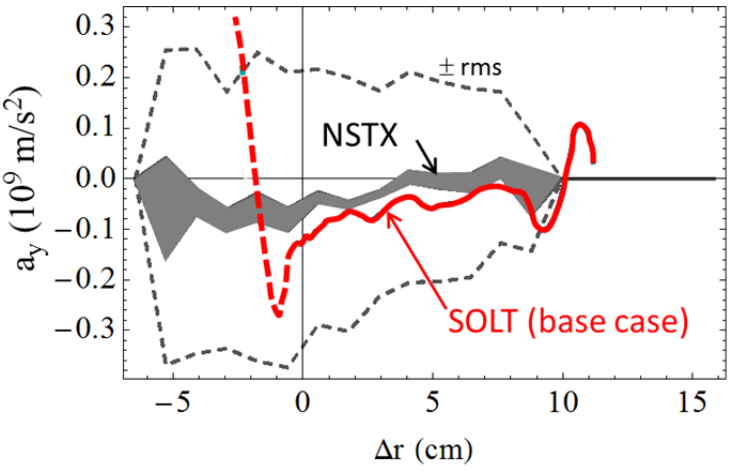

Figure 7. Reynolds acceleration $\langle a_y \rangle$ for seeded blob simulations compared with experimental results for NSTX. The grey curves are experimental data. The central shaded region is the mean acceleration, with statistical uncertainty. The dashed grey lines show the mean ± rms deviations for the experimental data. The red curve is from the SOLT seeded blob simulation with artificial initial transient shown by the dashed line.

Note that the typical values of a_y obtained here are of the order of magnitude v^2/ℓ, (where $v \sim 1$ km/s is a typical velocity and $\ell \sim 1$ cm is a typical scale length for the flows) indicating that the obtained accelerations are indeed significant. This is also evident by the fact the observed trajectories deviate strongly from purely ballistic motion.

The experimentally observed rms deviations in the velocity in Fig. 7 are large compared to the mean velocity. This indicates the presence of oscillating zonal flows, which can be considered as resulting from blob-blob interactions. Quasi-steady turbulence simulations (rather than the more straightforward seeded blob simulations) are required to further elucidate this. The SOLT turbulence simulations are compared with experimental results in Fig. 8 and show similar blob flows and accelerations as the experiment. The agreement in a_y of simulation with experiment is less precise than for the seeded blobs for two main reasons. Firstly, the turbulent system is not guaranteed to maintain the reference profiles to a high degree of accuracy. Secondly, the statistics of the blobs generated in the turbulence simulations is similar, but not identical, to those observed in the experiment. The turbulent simulations obviously provide a

more self-consistent description and capture large rms fluctuations of v_y and a_y relative to their means.

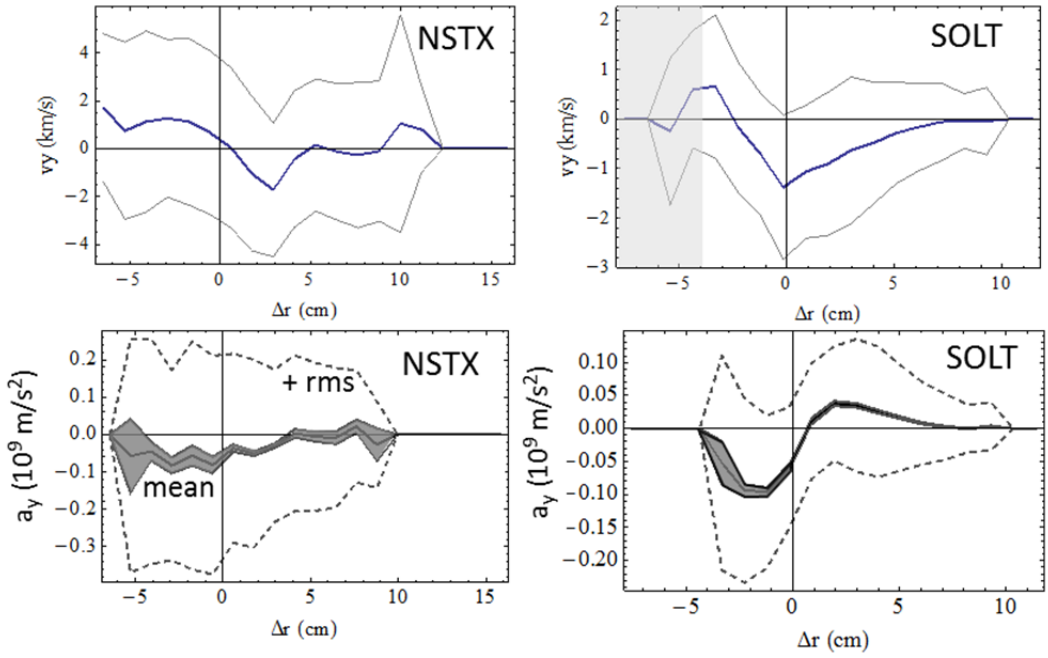

Figure 8. SOLT turbulence simulations (right) compared with NSTX data (left). Top panels are the mean blob v_y (thick blue) ± rms deviations (thin grey). The shaded region in the upper right SOLT figure may be influenced by the simulation boundary. Bottom panels are mean blob accelerations a_y (grey shading indicates statistical uncertainty) ± rms deviations (dashed).

D. Simulation comparisons for Alcator C-Mod

The NSTX case was a low collisionality case; now for contrast we consider a high collisionality case in Alcator C-Mod. An analysis of the blob accelerations for this C-Mod shot were carried out as previously described. The experimental database consisted of approximately 6,000 individual blob images (after filtering for an amplitude threshold of $\delta I/I > 0.2$, blob lifetimes > 25 μs, blob half-max area > 0.2 cm^2) and resulted in about 600 blob trajectories, which were employed to obtain Fig. 9.

For this highly collisional C-Mod case, SOLT simulations are more challenging because collisionality is expected to allow the blob-filaments to acquire structure (e.g. temperature gradients) along the magnetic field line. These gradients are allowed in the high collisionality (conduction limited) regime, but difficult to model in the 2D SOLT code.

When seeded blob simulations were carried out for the C-Mod case using midplane values, and no flow damping, significant a_y resulted, as shown by the green curve in Fig. 9. The C-Mod experimental result of near-zero mean a_y could be modeled satisfactorily only by making several additional assumptions (red curve): complete parallel sheath disconnection in the SOL, partial collisional disconnection in the edge, and finite flow damping, $\nu/\Omega_i = 0.02$. Theoretically, in our model, flow damping is equivalent to friction and also to extra charge dissipation by cross-field currents. [4,5] The latter are expected when X-points (and their associated thin radial fans [43, 44]) are present downstream along B. Friction could also be provided in this shot by neutral collisions [45]. With these simulation parameter choices, an acceleration is obtained that is close to the experimentally observed band.

SOLT turbulence simulations with these parameter choices are shown in Fig. 10. These simulations confirm the seeded blob results and qualitatively reproduce the experimental data: small mean flows and accelerations with significant rms fluctuations due to the turbulence.

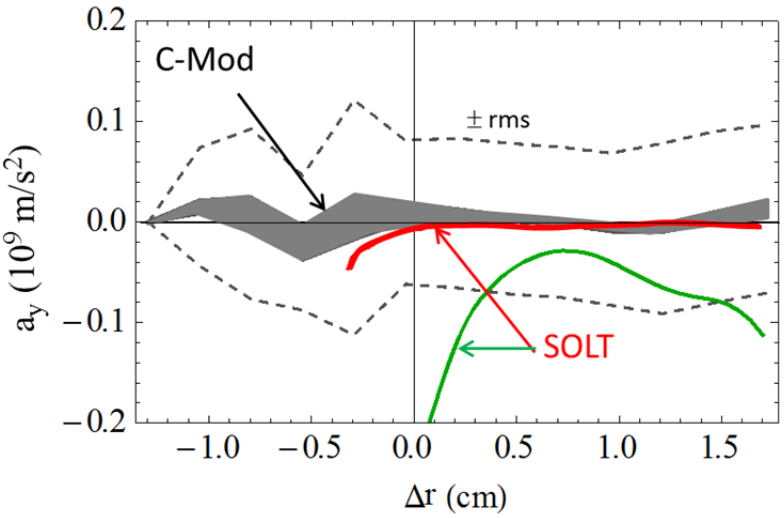

Figure 9. Reynolds acceleration $\langle a_y \rangle$ for seeded blob simulations compared with experimental results for Alcator C-Mod. The grey curves are experimental data. The central shaded region is the mean acceleration, with statistical uncertainty. The dashed grey lines show the mean ± rms deviations for the experimental data. The curves are from the SOLT seeded blob simulations showing the midplane test case (green), and the disconnected case with extra friction (red).

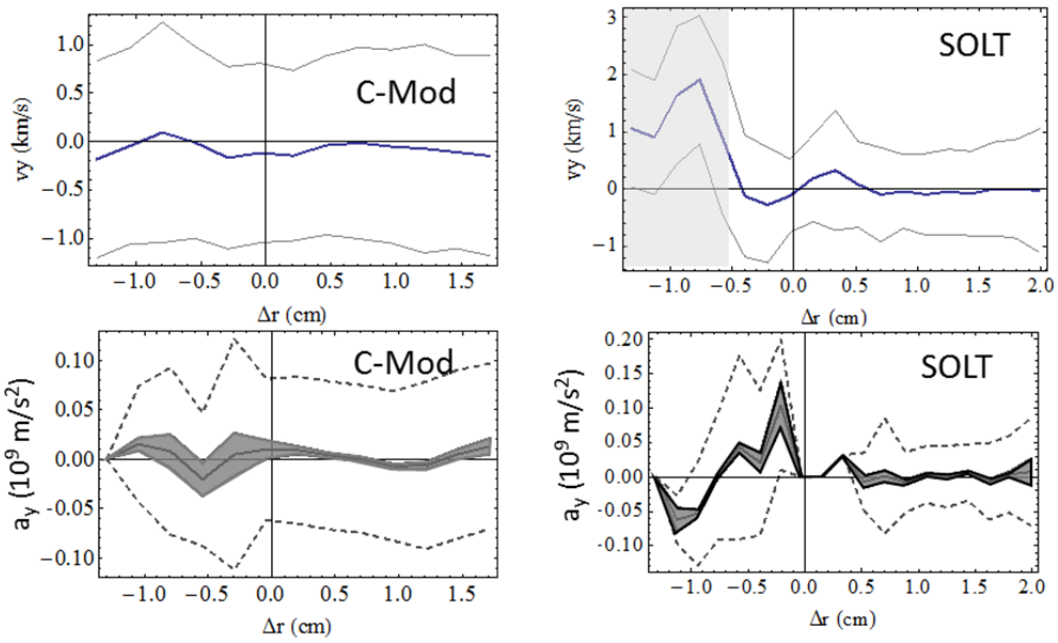

Figure 10. SOLT turbulence simulations (right) compared with Alcator C-Mod data (left). See Fig. 8 for a description of the curves.

E. Elliptical blob tilting and the Reynolds stress proxy

So far the Reynolds stress analysis in these discharges has relied on blob trajectories, but we also have information about the elliptical deformation of the structures. To analyze these deformations, we assume that the ellipticity and tilt angle of the blob electrostatic potential are similar to those of the density and temperature, and hence the GPI emission, notwithstanding possible detailed differences in internal structure. Given this assumption, it is shown in Appendix B that a normalized proxy for the Reynolds stress, hereafter referred to as the RSP, is given by

$$\mathrm{RSP} = -\sin(2\theta)[1-(r_2/r_1)^2] \qquad (2)$$

where θ is the tilt angle (measured clockwise from the positive ΔR or x axis) and r_2 (r_1) is the major (minor) axis of the best-fit ellipse. In the absence of either ellipticity or tilt, there is no Reynolds stress. See Figs. 11 a) and 11 b).

Figures 11 c) and e) show the results of an RSP analysis for the NSTX and Alcator C-Mod shots using experimental data. Each dot in these figures represents the shape and orientation vs. location of a blob at a particular time. The spatial derivative d/dx of the RSP is proportional to the Reynolds force. It follows that the mean Reynolds force for the NSTX shot is consistent with the observed direction of the mean blob flows in Fig. 8. For the C-Mod shot, the mean

Reynolds force is essentially zero, again consistent with the analysis in Fig. 9 and with the small flows observed in Fig. 10. A different analysis method of zonal flows for this (and other) Alcator C-Mod shots was described in Ref. [46]. Small mean zonal flows were also reported for this C-Mod shot (1100824017), and the oscillating zonal flows were found to have a broadband frequency spectrum.

Figures 11 d) and f) show the RSP analyses from the corresponding SOLT turbulence simulations for NSTX and C-Mod. Qualitative features of the experiment are reproduced, viz. radially varying structure of the RSP in the NSTX shot, and little in the C-Mod shot.

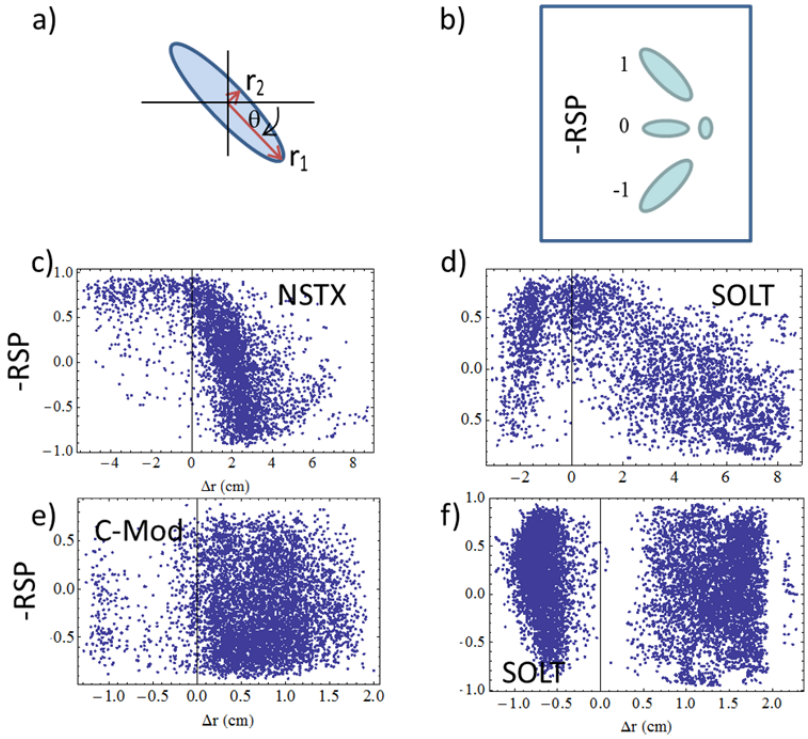

Figure 11. Reynolds stress proxy (RSP) definition and simulation-experiment comparisons: a) sketch of tilted elliptical blob and (r_1, r_2, θ) used in defining the RSP; b) sketch of blob shapes and orientations and the corresponding values of RSP; c) RSP for NSTX experimental data and d) for SOLT simulation; e) and f) C-Mod experimental data and corresponding SOLT simulation.

It is significant that for both the NSTX and C-Mod shots, an order unity variation of the RSP (essentially from -1 to 1, i.e. over the full possible range) is observed. This shows that significant instantaneous shearing stresses are acting on the blobs regardless of whether there are mean flows or not. In previous theoretical and simulation work [35] we showed that order unity shearing deformations of the blob structure are consistent with the idea that shearing affects the blob dynamics, i.e. $\omega'_E \sim \gamma \sim 1/\tau_c$ where γ is a characteristic linear growth rate or inverse auto-

correlation time, and ω'_E is the shearing rate. When the shearing rate is of this magnitude or larger, it both creates isolated blob structures from radial streamers [35, 47] and begins to suppress turbulent radial transport, e.g. consistent with the discussion of Fig. 6f).

The presence of time-dependent flows as well as mean flows in these simulations is suggested by the large rms deviations apparent in Figs. 8 and 10, as well as by the large spread in RSP in Fig. 11. The time-dependent flows are further illustrated by the single-point frequency spectrum of v_{Ey} show in Fig. 12 for NSTX. (Spectra for the C-Mod case are qualitatively similar.) The spectrum is shown at the separatrix location, where from Fig. 8 (upper right) we see that the mean flow and the rms deviation are almost equal. This spectrum in Fig. 12, which is typical of both density and velocity fluctuations in the present simulations, is also qualitatively similar to experimental data (see e.g. Fig. 9 of Ref. [8]). Note the approximate power law dependence in each of two separate bands, here 2 – 30 kHz and f > 30 kHz. The 30 kHz breakpoint corresponds roughly to the inverse auto-correlation time (self-transit time) of a blob ($v_b/\delta_b \sim 1/\tau_c$) while the 2 kHz rate is a typical rate at which the source functions refuel the core region after a blob loss event. The inset plot is on a linear scale and emphasizes low frequency (f < 5 kHz) oscillations that are sometimes seen and related to zonal flows. Figure 12 clearly indicates that low frequency flows exists in addition to the zero frequency (mean) flows. Theoretical work [3, 10, 48] suggests that both types of flows are of interest for interaction with turbulence, and may even be competitive [48].

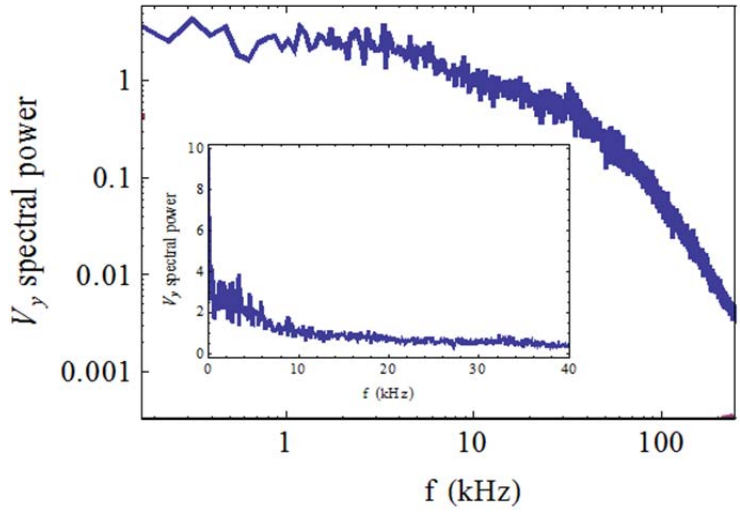

Figure 12. Single point frequency spectrum of v_{Ey} taken at the separatrix from SOLT code simulations of the NSTX shot. The inset shows the 0 – 40 kHz spectrum on a linear scale.

F. Turbulent flow generation and net force

Encouraged by the qualitative agreement of SOLT turbulence simulations with the experimental results shown in Figs. 7 – 11, we can employ the simulations to calculate quantities not directly available from the data. One such quantity that is frequently of interest [49] is the turbulence production rate

$$P_t = -\left\langle v_x v_y \right\rangle \frac{\partial \left\langle v_y \right\rangle}{\partial x} \tag{3}$$

where the zonal averages <…> are taken over the y-coordinate at each time point, and the entire expression is then time-averaged to obtain a mean and its corresponding rms fluctuations. The result for NSTX, shown in Fig. 13., indicates $P_t < 0$, i.e. energy is being transferred from the turbulence to the mean flows as expected. P_t has dimensions of v^2/τ. Taking a typical velocity as 1 km/s (see e.g. Fig. 8) and a typical blob time-scale as $\tau_c \sim 30$ μs, a characteristic order-of-magnitude is $v^2/\tau_c \sim 0.3\times10^{15}$ cm^2/s^3. Consequently, the observed $P_t \sim 10^{15}$ cm^2/s^3 is significant. Free energy in the pressure gradient generates turbulent energy which is then partially transferred to mean flows.

Results for P_t in the high collisionality C-Mod shot (not shown) are qualitatively similar in shape, but the order of magnitude is much smaller $\sim 10^{12}$ cm^2/s^3 indicating a negligible transfer of energy to mean flows for this shot; this is consistent with the much smaller mean flows that are observed.

Of course the turbulence, which manifests itself in the outwardly ejected blobs (Fig. 2), implies particle, momentum, and heat fluxes across the separatrix. The transport of momentum across the separatrix results in a net force on the plasma. The strength of this force per unit of power flowing across the separatrix is given by the ratio of momentum to heat flux:

$$\frac{F_\perp}{P} = \frac{\left\langle n v_x v_y \right\rangle}{\left\langle 2 n T v_x \right\rangle} \tag{4}$$

where here $P = P_{sep}$ is power (not to be confused with P_t), and in the expression for the heat flux, the factor of 2 accounts for the ion contribution assuming $T_e = T_i$. From the simulations, we estimate the perpendicular force on the plasma as $F_\perp/P = 0.8$ N/MW for the NSTX shot, and $F_\perp/P < 0.05$ N/MW for the C-Mod shot.

When projected onto the toroidal direction, $F_\perp$ contributes to the so-called intrinsic torque driving toroidal rotation. In order-of-magnitude the 1 N/MW level is similar to values obtained near the separatrix on DIII-D [50]. Because of the simplified non-toroidal geometry of the SOLT model, we cannot claim that this effect explains intrinsic toroidal rotation, but it would appear to represent a competitive effect that cannot be ignored. Furthermore, the torque exists in

the absence of background E_r driven flows as illustrated in Figs. 6a) – 6d), and therefore qualifies as a symmetry-breaking or residual Reynolds stress.

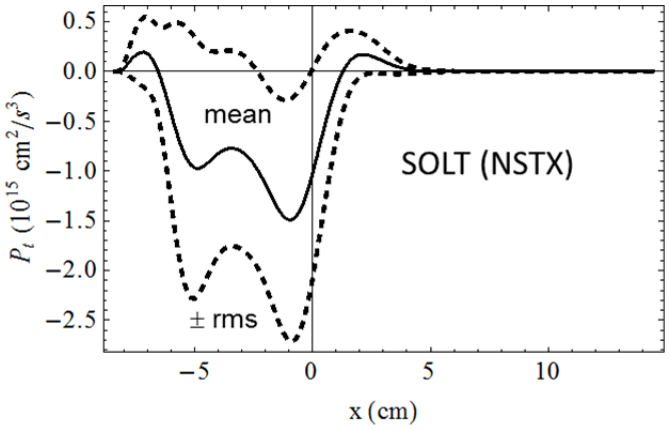

Figure 13. Turbulence production rate P_t from the SOLT simulation of the NSTX shot showing the mean value (solid) and mean ± rms deviations (dashed). $P_t < 0$ implies turbulent energy is being transferred to mean flows.

5. Discussion and conclusions

A combination of experimental data analysis, seeded blob simulations, and turbulence simulations have been employed to study the interaction of blob-filaments with sheared flows. Here we consider a rather general definition of blob-filaments that includes both isolated wave crests in the edge region, and structures that have been ejected into the SOL. Theoretical mechanisms related to radial inhomogeneity, and parallel sheath currents from radial changes in magnetic topology cause the generation of Reynolds stress, including a so-called residual Reynolds stress that is non-zero even when there are no background **E**×**B** flows. An important conclusion, illustrated in Figs. 7 and 8, is that these mechanisms are sufficient to explain the observed Reynolds acceleration and hence the generation of blob perpendicular (approximately poloidal) flows (their size, radial scale, direction and reversal across the separatrix) in a low collisionality NSTX shot. A selected high collisionality Alcator C-Mod shot shows very small mean sheared flows. It was found (see Fig. 9) that many characteristics of this shot could be simulated by additionally assuming (i) collisional disconnection of the midplane from the divertor sheaths, and (ii) flow damping or equivalently charge dissipation by radial currents, possibly due to X-point effects. In both the NSTX and C-Mod cases mean and oscillating zonally averaged flows are sufficiently strong to affect blob dynamics and transport, as shown by

the blob trajectories and resulting accelerations (Figs. 7 and 9) and the elliptical deformation of the blob structures (Fig. 11).

The studies described here have implications for SOL interactions of blobs with plasma facing components. As evidenced by Figs. 6e) and 6f), blob trajectories, and their radial (x) penetration into the SOL are influenced by their motion in the binormal (y) direction, and in particular by the flow shear in the near-separatrix region. The near-SOL heat flux width may be set by the radial penetration of blob-filaments into the SOL, arising from a competition between the radial blob velocity and the parallel expansion velocity of heat towards the divertor plates. Judiciously driven sheared flows in the SOL could increase the SOL width, likely at the expense of edge confinement, such as the "reverse" flows shown in Fig. 6e) which enhance the blob ejection velocity due to polarization charge interactions. These flows could be produced by toroidally symmetric biasing, in contrast to the toroidally dependent biasing studied elsewhere. [51-53]

There are also implications for understanding L-H transition physics. Recent work has advanced the hypothesis that mean and oscillating zonal flows build up in the L-mode phase as additional heating power is applied, until eventually transport suppression triggers profile steepening, and an H-mode phase in which sheared **E**×**B** flows are maintained by the role of the large ion pressure gradient in radial force balance. The present studies add to this picture by showing how seed flows are initially established in Ohmic plasmas.

While our work has concentrated on perpendicular forces and flows, there are clearly implications for toroidal torques and flows near the separatrix and in the SOL. Because our model does not contain all relevant toroidal effects, we can only say the toroidal projection of the perpendicular dynamics discussed here is likely to be a significant contributor in the toroidal direction. Recent work [33] has identified a theoretical mechanism relevant to toroidal flows which changes sign when the X-point topology is changed relative to the grad-B drift direction. On the other hand, the residual stress mechanism discussed here in connection with Fig. 6, and responsible for the forces producing Fig. 13, may play a role in setting up a component of toroidal plasma rotation which does not change when X-point topology is changed. Both types of flows have been observed [54]; the latter is essentially a toroidal rotation of the SOL in the co-current direction that is strong at low densities and weaker at high densities.

Aside from these more speculative implications, the main results of our paper are to be found in Figs. 3, 6 and 7 which illustrate the mechanisms responsible for flow generation by blob-filament dynamics in the near-separatrix region and the simulated comparisons of those mechanisms with experimental data. While the simulation model employed here has many caveats, such as cold ions, 2D fluid theory, and the use of a simplified drift-wave physics model, it does captures the essence of nonlinear polarization and **E**×**B** dynamics in the separatrix region,

and those essentials would appear to be sufficient as a framework for understanding many aspects of the experimental data.

Acknowledgments

The authors thank the NSTX and Alcator C-Mod teams for their contributions to tokamak operations which enabled collection and analysis of the data employed here. In particular, we thank R. J. Maqueda for taking the GPI data on NSTX, B. Cao for a discussion of camera calibration, and S. Gerhardt for assistance in determination of the separatrix location in the NSTX shot. This work was supported by the US DOE under grants DE-FG02-97ER54392, DE-FG02-02ER54678, DE-AC02-09-CH11466, DE-FC02-99ER54512, DE-AC02-09CH11466, and PPPL Subcontract S009625-F.

Appendix A: The SOLT model

Computations are carried out with the 2D Scrape-Off-Layer Turbulence (SOLT) code [35]. Analytical closure relations are employed to describe the parallel dynamics. For example, the relationship of parallel current $J_{||}$ to Φ is prescribed by a sheath closure on open field lines (generalized to allow for collision-dominated regimes), and a Wakatani-Hasegawa-like model [55] for $J_{||}$ is employed on closed field lines to capture basic drift-wave physics.

The fundamental equations for the SOLT model are the vorticity, continuity and energy conservation (or alternatively temperature) equations

$$\frac{d}{dt}\nabla\cdot n\nabla\Phi = A_{dw}(\Phi,n) + \alpha_{sh}J_{||} - \beta\frac{\partial(nT)}{\partial y} \tag{A1}$$

$$\frac{dn}{dt} = A_{dw}(\Phi,n) - \alpha_{sh}\left(nT^{1/2} - J_{||}\right) \tag{A2}$$

$$\frac{dT}{dt} = -\alpha_{sh}\frac{q_{||}}{n} \tag{A3}$$

Here we employ dimensionless notation (using the Bohm normalization with time-scale $\Omega_{ci} = ZeB/m_ic$ and space scale $\rho_{sr} = c_{sr}/\Omega_{ci}$ where $c_{sr}^2 = T_{er}/m_i$ and T_{er} is a reference temperature for the normalization). The simulation plane is denoted as the (x, y) plane where x is the radial direction and y is binormal (approximately poloidal). The convective derivative is written as $d/dt = \partial/\partial t + \mathbf{v}\cdot\nabla$ where $\mathbf{v} = \mathbf{e}_z\times\nabla\Phi$. A_{dw} is the drift wave operator

$$A_{dw}(\Phi,n) = \alpha_{dw}\overline{T}^{3/2}\{\Phi - T\ln n\} \tag{A4}$$

$$\alpha_{dw} = \frac{2k_{||}^2v_{te}^2}{\nu_{ei}\Omega_i} \tag{A5}$$

where for any quantity Q, $\langle Q \rangle \equiv \overline{Q}$ denotes the zonal or y average part and $\widetilde{Q} \equiv \{Q\} \equiv Q - \overline{Q}$ denotes the fluctuating part. Thus A_{dw} enforces a Boltzmann response on fluctuations when the coefficient α_{dw} is large, in the spirit of the Wakatani-Hasegawa adiabaticity parameter. Note that the flux-surface or y-average of A_{dw} vanishes (as it must since it arises from $\nabla_{||} J_{||}$ on closed surfaces).

Other coefficients appearing in the model are: the sheath conductivity parameter

$$\alpha_{sh} = \frac{\rho_{sr}}{L_{||}} \tag{A6}$$

where $L_{||}$ is the midplane-to-divertor-plate connection length in the SOL and ρ_{sr} is the reference sound gyro-radius, and the curvature drive parameter

$$\beta = \frac{2\rho_{sr}}{R} \tag{A7}$$

where R is the effective radius of curvature (approximately the major radius of the torus).

To close the system of equations, the parallel current and heat flux $J_{||}$, $q_{||}$ must be expressed in terms of the dynamic variables Φ, n and T. A set of closure relations, valid for a range of collisionality regimes from conduction limited to sheath-connected, is employed here. In the sheath-connected limit the parallel current and heat flux are given by

$$J_{||SL} = nT^{1/2}\left(1 - e^{(\Phi_B - \Phi)/T}\right) \tag{A8}$$

$$q_{||SL} = s_E\, nT^{3/2} e^{(\Phi_B - \Phi)/T} \tag{A9}$$

where $\Phi_B \sim 3$ T, and $s_E \sim 6$ is the sheath energy transmission factor. In the collisional (conduction limited) case we employ

$$J_{||CL} = \frac{1.96 nT^{1/2}}{\Lambda} \frac{(\Phi_B - \Phi)}{T} \tag{A10}$$

$$q_{||CL} = \frac{3.2 nT^{3/2}}{\Lambda} \tag{A11}$$

where the collisionality parameter Λ is given by

$$\Lambda = \frac{\nu_{ei} L_{||}}{\Omega_e \rho_s} \tag{A12}$$

Λ is related to the SOL electron parameter ν_{*e} introduced by some authors as $\nu_{*e} = L_{||}/\lambda_{ei} = \Lambda (m_i/m_e)^{1/2}$, where λ_{ei} is the electron mean free path for collisions with ions. These parallel closures are Padé-interpolated to provide a smooth connection between the sheath and conduction limited cases. Flux limits are also imposed. See Ref. [39] for a discussion of additional details.

The SOLT code solves the vorticity equation, by splitting Eq. (A1) into zonally-averaged and fluctuating parts. The zonally-averaged part is manipulated into a conservative form for

zonal (i.e. y) momentum conservation. The Boussinesq approximation is employed on the fluctuating part. Small diffusive terms (respectively $\mu\nabla^4\Phi$, $D_n\nabla^2 n$, $D_T\nabla^2 T$) are usually added to the right-hand sides of Eqs. (A1) – (A3) to absorb high-wavenumber fluctuations before they cascade to the scale of the numerical grid. A friction term ($-\nu\nabla^2\Phi$) can also be added to the vorticity equation to model Alfven wave emission, neutral collisions and other frictional dissipative effects. Further discussion of the SOLT model is given in previous publications [35].

Finally, particle and heat sources are added to the density and temperature equations for the turbulence simulations, in order to allow a quasi-steady state to be maintained in the presence of SOL losses. For the analysis of experimental shots, the sources are implemented by relaxing the turbulent n and T profiles to reference target values obtained from the experiment, such as those shown in Fig. 4. The ad-hoc source relaxation rates are typically chosen to be of order c_s/R in the edge, and are taken smoothly to zero in the SOL.

The simulations in this paper employed the following dimensionless parameters: for the NSTX base case seeded blob simulations $\beta = 0.0060$, $D_n = D_T = 0$, $\mu = 0.2$, $\nu = 0$, $\alpha_{dw0} = 0.083$, Zeff = 2, and $\alpha_{sh5} = 0.00105$ (i.e. the value at x = 5 cm, see Fig. 4 for profiles); for the NSTX turbulence simulations, parameters were the same except that $D_n = D_T = 0.001$, a smaller value of $\mu = 0.05$ was employed to permit sustained turbulence, and the effective connection length was arbitrarily reduced by a factor of 2 to give $\alpha_{sh5} = 0.00052$ to prevent an excessive (and experimentally unobserved) buildup of density in the SOL. For the C-Mod base case seeded blob simulations (midplane parameters yielding the green curve in Fig. 9) $\beta = 0.00089$, $D_n = D_T = 0$, $\mu = 0.2$, $\nu = 0$, $\alpha_{dw0} = 0.0076$, Zeff = 2, and $\alpha_{sh1} = 6.5\times10^{-5}$; the disconnected frictional case (red curve in Fig. 9) modified the parameters to $Z_{eff} = \infty$, $\alpha_{dw0} = 0.0019$, $\nu = 0.02$; and the turbulence simulations employed the later parameter set with in addition $D_n = D_T = 0.001$.

Appendix B: The Reynolds stress proxy (RSP)

The idea and central assumption behind the RSP is that the eddy structures of electrostatic potential have the same shape and orientation as the GPI images. Under this assumption, is it possible to form the Reynolds stress $\langle v_x v_y \rangle$ from the elliptical equipotential flow contours and average it around the ellipse to obtain a proxy for the Reynolds stress.

Let

$$\Phi = \Phi(g) \tag{B1}$$

where

$$\frac{\xi^2}{r_1^2} + \frac{\eta^2}{r_2^2} = g^2 \tag{B2}$$

and the rotated coordinates ξ and η are defined by the r_1 and r_2 directions in Fig. 11a) so that

$$\xi = x\cos(\hat{\theta}) + y\sin(\hat{\theta}) \tag{B3}$$

$$\eta = y\cos(\hat{\theta}) - x\sin(\hat{\theta}) \tag{B4}$$

where, for convenience we let $\hat{\theta} = -\theta$. The E×B velocities are

$$v_x = -\frac{\partial \Phi}{\partial y} \tag{B5}$$

$$v_y = \frac{\partial \Phi}{\partial x} \tag{B6}$$

therefore, using the chain rule, e.g.

$$\frac{\partial \Phi}{\partial x} = \frac{d\Phi}{dg}\frac{\partial g}{\partial x} = \frac{d\Phi}{dg}\left(\frac{\partial g}{\partial \xi}\frac{\partial \xi}{\partial x} + \frac{\partial g}{\partial \eta}\frac{\partial \eta}{\partial x}\right) \tag{B7}$$

with

$$\frac{\partial g}{\partial \xi} = \frac{\xi}{g r_1^2} \tag{B8}$$

$$\frac{\partial g}{\partial \eta} = \frac{\eta}{g r_2^2} \tag{B9}$$

one obtains

$$v_x = -\frac{1}{g}\frac{d\Phi}{dg}\left(\frac{\xi}{r_1^2}\sin\hat{\theta} + \frac{\eta}{r_2^2}\cos\hat{\theta}\right) \tag{B10}$$

$$v_y = \frac{1}{g}\frac{d\Phi}{dg}\left(\frac{\xi}{r_1^2}\cos\hat{\theta} - \frac{\eta}{r_2^2}\sin\hat{\theta}\right) \tag{B11}$$

The next step is to parameterize distance around the ellipse by an angle φ

$$\xi = g r_1 \cos\varphi \tag{B12}$$

$$\eta = g r_2 \sin\varphi \tag{B13}$$

so that

$$v_x = -\frac{d\Phi}{dg}\left(\frac{\cos\varphi\sin\hat{\theta}}{r_1} + \frac{\sin\varphi\cos\hat{\theta}}{r_2}\right) \tag{B14}$$

$$v_y = \frac{d\Phi}{dg}\left(\frac{\cos\varphi\cos\hat{\theta}}{r_1} - \frac{\sin\varphi\sin\hat{\theta}}{r_2}\right) \tag{B15}$$

We introduce the average over φ

$$< ... >= \int \frac{d\varphi}{2\pi}(...) \tag{B16}$$

to obtain

$$< v_x v_y >= \frac{1}{4 r_2^2}\left(\frac{d\Phi}{dg}\right)^2 \sin 2\hat{\theta}\left(1 - \frac{r_2^2}{r_1^2}\right) \tag{B17}$$

Thus, an un-normalized proxy for the RS $\propto <v_x v_y>$, in terms of the original angle θ, is

$$RS = -\sin 2\theta\left(1 - \frac{r_2^2}{r_1^2}\right) \tag{B18}$$

Reference

[1] Diamond P. H., et al., 2005 Plasma Phys. Control. Fusion **47** R35

[2] Diamond P. H. and Kim Y.-B., 1991 Fluids B **3** 1626

[3] Terry P. W. 2000 Rev. Mod. Phys. **72** 109

[4] Krasheninnikov S. I., et al., 2008 J. Plasma Physics **74** 679

[5] D'Ippolito D. A., et al., 2011 Phys. Plasmas **18** 060501

[6] Maqueda R.J., et al., 2001 Rev. Sci. Instrum., **72** 931

[7] Zweben S. J., et al., 2004 Nucl. Fusion **44** 134

[8] Terry J. L., et al., 2003 Phys. Plasmas **10** 1739

[9] Kim E. J. and Diamond P. H., 2003 Phys. Rev. Lett. **90** 185006

[10] Malkov M. A. and Diamond P. H., 2009 Phys. Plasmas **16** 012504

[11] Delgado J. M., Garcia L. and Carreras B. A., 2009 Plasma Phys. Control. Fusion **51** 015003

[12] Zweben S. J., et al., 2010 Phys. Plasmas **17** 102502

[13] Conway G. D., et al., 2011 Phys. Rev. Lett. **106** 065001

[14] LaBombard B., et al., 2005 Phys. Plasmas **12** 056111

[15] Schmitz L., et al., 2012 Phys. Rev. Lett. **108** 155002

[16] Estrada T., Hidalgo C., Happel T., and. Diamond P. H, Phys. 2011 Rev. Lett. **107** 245004

[17] Xu G. S., et al., 2011 Phys. Rev. Lett. **107** 125001

[18] Tynan G.R., et al., in *Proceedings of the 24th IAEA Fusion Energy Conference*, San Diego, USA, 2012, IAEA-CN-197-EX/10-3.

[19] Xu M., et al., 2012 Phys. Rev. Lett. **108** 245001

[20] Lipschultz, B., et al., 2007 Nucl. Fusion **47** 1189

[21] Loarte A. et al., 2007 Nucl. Fusion **47** S203

[22] Yu G. Q. and Krasheninnikov S. I., 2003 Phys. Plasmas **10** 4413

[23] Ghendrih Ph., et al., 2003 Nucl. Fusion **43** 1013

[24] Myra J. R., D'Ippolito D. A., Krasheninnikov S. I. and Yu G. Q., 2004 Phys. Plasmas **11** 4267

[25] Windisch T., Grulke O., Naulin V. and Klinger T., 2011 Plasma Phys. Control. Fusion **53** 124036

[26] Diallo A., Fasoli A., Furno I., Labit B., Podestà M. and Theiler C., 2008 Phys. Rev. Lett. **101** 115005

[27] Sechrest Y., et al., 2011 Phys. Plasmas **18** 012502

[28] Alonso J.A. et al., 2012 Nucl. Fusion **52** 063010

[29] Alonso J.A. et al., 2013 Plasma Phys. Control. Fusion **55** 014001

[30] Alonso J.A. et al., 2006 Plasma Phys. Control. Fusion **48** B465

[31] Shesterikov I., et al. 2012 Nucl. Fusion **52** 042004

[32] Fedorczak N., et al., 2012 Phys. Plasmas **19** 072314

[33] Fedorczak N., Diamond P.H., Tynan G. and Manz P., 2012 Nucl. Fusion **52** 103013

[34] Davis W. M., et al., *54th Annual Meeting of the APS/DPP*, 2012, Providence, RI., paper YP8.00038.

[35] Russell D. A., Myra J. R. and D'Ippolito D. A., 2009 Phys. Plasmas **16** 122304

[36] N. Bisai, R. Singh, and P. K. Kaw, 2012 Phys. Plasmas **19** 052509

[37] Angus J. R., Krasheninnikov S. I., and Umansky M. V., 2012 Phys. Plasmas **19** 082312

[38] Furno, I., et al., 2011 Plasma Phys. Control. Fusion **53** 124016

[39] Myra, J. R., et al., 2011 Phys. Plasmas **18** 012305

[40] Cziegler I., Terry J. L., Hughes J. W., and LaBombard B., 2010 Phys. Plasmas **17** 056120

[41] Burrell K., 1997 Phys. Plasmas **4** 1499

[42] Agostini M., et al., 2007 Phys. Plasmas **14** 102305

[43] Farina D., et al., 1993 Nucl. Fusion **33** 1315

[44] Terry J.L., et al., 2009 J. Nucl. Mater **390–391** 339

[45] Katz N., et al., 2008 Phys. Rev. Lett. **101** 015003

[46] Zweben S. J., et al., 2012 Plasma Phys. Control. Fusion **54** 025008

[47] Bisai N., et al., 2005 Phys. Plasmas **12** 072520; and 2005 Phys. Plasmas **12** 102515.

[48] Zhang Y. Z., Xie T., and Mahajan S. M., 2012 Phys. Plasmas **19** 020701

[49] Manz P., et al., 2012 Phys. Plasmas **19** 072311

[50] Műller S. H., et al., 2011 Phys. Rev. Lett. **106** 115001

[51] Cohen R.H. and Ryutov D.D., 1997 Nucl. Fusion **37** 621

[52] Zweben S.J., et al., 2012 Plasma Phys. Cont. Fusion **54** 105012

[53] Theiler C., et al., 2012 Phys. Plasmas **19** 082305

[54] LaBombard, B., et al., 2004 Nucl. Fusion **44** 1047

[55] Wakatani M. and Hasegawa A. 1984 Phys. Fluids **27** 611